



# Electron and Proton Energization in 3D Reconnecting Current Sheets in Semirelativistic Plasma with Guide Magnetic Field

Gregory R. Werner<sup>1</sup> and Dmitri A. Uzdensky<sup>1</sup>Center for Integrated Plasma Studies, Physics Department, 390 UCB, University of Colorado, Boulder, CO 80309, USA; [Greg.Werner@colorado.edu](mailto:Greg.Werner@colorado.edu)*Received 2023 November 22; revised 2024 February 26; accepted 2024 March 2; published 2024 March 22*

## Abstract

Using 3D particle-in-cell simulation, we characterize energy conversion, as a function of guide magnetic field, in a thin current sheet in semirelativistic plasma, with relativistic electrons and subrelativistic protons. There, magnetic reconnection, the drift-kink instability (DKI), and the flux-rope kink instability all compete and interact in their nonlinear stages to convert magnetic energy to plasma energy. We compare fully 3D simulations with 2D in two different planes to isolate reconnection and DKI effects. In zero guide field, these processes yield distinct energy conversion signatures: ions gain more energy than electrons in 2D<sub>xy</sub> (reconnection), while the opposite is true in 2D<sub>yz</sub> (DKI), and the 3D result falls in between. The flux-rope instability, which occurs only in 3D, allows more magnetic energy to be released than in 2D, but the rate of energy conversion in 3D tends to be lower. Increasing the guide magnetic field strongly suppresses DKI, and in all cases slows and reduces the overall amount of energy conversion; it also favors electron energization through a process by which energy is first stored in the motional electric field of flux ropes before energizing particles. Understanding the evolution of the energy partition thus provides insight into the role of various plasma processes, and is important for modeling radiation from astrophysical sources such as accreting black holes and their jets.

*Unified Astronomy Thesaurus concepts:* [Plasma astrophysics \(1261\)](#); [High energy astrophysics \(739\)](#); [Active galactic nuclei \(16\)](#); [Plasma physics \(2089\)](#); [Astrophysical black holes \(98\)](#); [Magnetic fields \(994\)](#)

## 1. Introduction

In many plasma environments, magnetic energy is converted to plasma energy at thin current sheets (CSs), likely via magnetic reconnection (e.g., Zweibel & Yamada 2009). Reconnection occurs in diverse regimes and, even in 2D, generates such complexity that we owe much of our understanding to numerical simulation. Unfortunately, 3D simulation studies are far costlier than 2D, motivating efforts to understand similarities between 2D and 3D reconnection and more generally to understand 3D CS evolution in terms of 2D processes whenever possible.

A thin CS, considered in 2D (specifically in “2D<sub>xy</sub>,” the  $x$ - $y$  plane perpendicular to the current  $j_z$  supporting a magnetic field  $\hat{x}B_0 \tanh(y/\delta)$  reversing over thickness  $2\delta$ ), will typically be most unstable to tearing, leading, in its nonlinear stage, to reconnection and rapid magnetic energy release. In 2D<sub>yz</sub>, the same CS may kink or ripple due to the drift-kink instability (DKI), which in its nonlinear stage induces severe contortions that rapidly release magnetic energy (e.g., Pritchett et al. 1996). The DKI requires two counterdrifting species and hence is not a magnetohydrodynamic (MHD) instability; it is important when the separation between electron and ion scales is small (Daughton 1999; Hesse & Birn 2000; Scholer et al. 2003), or absent as in relativistic pair plasma (Zenitani & Hoshino 2005, 2008; Yin et al. 2008; Liu et al. 2011; Cerutti et al. 2014; Guo et al. 2014, 2015). In 3D, these instabilities can compete and interact. Although 2D-like reconnection may dominate DKI in 3D (Kagan et al. 2013; Cerutti et al. 2014; Guo et al. 2014, 2015, 2021; Sironi & Spitkovsky 2014; Werner &

Uzdensky 2017), Werner & Uzdensky (2021) highlighted how the DKI can dramatically slow reconnection. Furthermore, in 3D only, flux ropes formed by reconnection can decay via the MHD kink instability (Kagan et al. 2013; Markidis et al. 2014; Zhang et al. 2021b; Schoeffler et al. 2023), releasing additional magnetic energy (Werner & Uzdensky 2021).

Using particle-in-cell (PIC) simulation, this work characterizes energy conversion as a function of guide magnetic field, in 3D CSs in magnetically dominated, collisionless electron–proton plasma, with true mass ratio  $\mu = 1836$ , in the semirelativistic regime. In semirelativistic plasma, where electrons are ultrarelativistic and protons subrelativistic, relativistic effects diminish the scale separation between (e.g., gyroradii of) electrons and ions (protons), making DKI consequential. The semirelativistic regime is one of the several important regimes for black hole (BH) accretion flows, which are expected to have electron–ion plasma at temperatures around 10–100 MeV (e.g., Dexter et al. 2020) and likely develop large, complicated, turbulent magnetic field structures in the accretion flow, in the overlying corona/wind, and in and around the jet (e.g., Galeev et al. 1979; Uzdensky & Goodman 2008; Ripperda et al. 2020; Chashkina et al. 2021; Bacchini et al. 2022; Zhbankin et al. 2023). We generally expect CS formation and reconnection in such contexts, and the resulting particle energization could potentially power flaring emission in BHs (as in solar flares). Furthermore, characterizing electron and ion energization in the semirelativistic regime is crucial for global MHD modeling of reconnection-powered emission from accreting BHs (Chael et al. 2018; Dexter et al. 2020; Ressler et al. 2020, 2023; Hankla et al. 2022; Scepi et al. 2022).

Until now (to our knowledge), no 3D PIC studies of electron–ion reconnection (or CS evolution) have characterized energy conversion in the nonradiative semirelativistic regime



Original content from this work may be used under the terms of the [Creative Commons Attribution 4.0 licence](#). Any further distribution of this work must maintain attribution to the author(s) and the title of the work, journal citation and DOI.

**Table 1**  
Initial Plasma and Numerical Simulation Parameters

$\mu \equiv m_i/m_e = 1836$	ion/electron mass ratio
$B_0$	asymptotic upstream (reversing) magnetic field
$n_b = n_{be} = n_{bi}$	background electron/ion density
$T_b = 18.36m_e c^2 = 0.01m_i c^2$	background electron/ion temperature
$\sigma_i \equiv B_0^2/(4\pi n_b m_i c^2) = 0.5$	background ion cold magnetization
$\sigma_e \equiv B_0^2/(4\pi n_b m_e c^2) = \mu\sigma_i = 918$	background electron cold magnetization
$\delta = 0.33\sigma_i\rho_{i0}$	Harris CS half-thickness ( $\rho_{i0} \equiv m_i c^2/eB_0$ )
$\mathbf{B}(y) = \hat{z}B_{gz} - \hat{x}B_0 \tanh(y/\delta)$	magnetic field profile
$-0.6c\hat{z}, +0.0004c\hat{z}$	electron, ion bulk drift velocities in CS
$\eta \equiv n_{d,\max}/n_b = 5$	CS overdensity
$n_d(y) = \eta n_b \cosh^2(y/\delta)$	CS electron/ion density profile
$T_d = 51m_e c^2 = 0.28m_i c^2$	CS electron/ion (comoving) temperature
$\beta_{be} = \beta_{bi} \equiv 8\pi n_b T_b/B_0^2 = 0.04$	upstream plasma beta for electrons/ions
$v_A = 0.57c$	upstream Alfvén velocity for $B_{gz} = 0$
$L_y \equiv L = 55.3\sigma_i\rho_{i0}$	system size (in $y$ )
$L_x/L = 1$	system $x/y$ aspect ratio (for 2D $xy$ and 3D)
$L_z/L = \max(1, B_{gz}/B_0)$	system $z/y$ aspect ratio (for 2D $yz$ and 3D)
$T = 20L/c$	simulation duration
$\Delta y = \Delta z = 0.036\sigma_i\rho_{i0}$	grid cell size in $y$ and $z$
$\Delta x = 0.058\sigma_i\rho_{i0}$	grid cell size in $x$
$\Delta t = 0.64\Delta y/c$	time step (the 3D Courant–Friedrichs–Lewy maximum)
$M_{\text{ppcs}} = 10$ (3D), 160 (2D)	macroparticles per cell per species (four species)
$M_{\text{ppcs}} = 40$ (3D), 640 (2D)	total macroparticles per cell

**Table 2**  
Initial Length Scales Normalized to  $\sigma_i\rho_{i0} = \sigma_e\rho_{e0}$ , where  $\rho_{s0} = m_s c^2/eB_0$ ,  $\sigma_s = B_0^2/(4\pi n_{bs} m_s c^2)$

$\Delta y = \Delta z$	0.036	grid cell size in $y, z$
$\Delta x$	0.058	grid cell size in $x$
$\rho_{be}$	0.060	upstream electron gyroradius ( $B_{gz} = 0$ )
$\lambda_{De} = \lambda_{Di}$	0.14	upstream electron/ion Debye length
$d_e$	0.25	upstream relativistic electron skin depth
$\delta$	0.33	CS half-thickness
$\rho_{bi}$	0.35	upstream ion gyroradius ( $B_{gz} = 0$ )
$\sigma_e\rho_{e0}$	1.0	twice the energized electron gyroradius, if all magnetic energy went to electrons
$d_i$	1.4	upstream nonrelativistic ion skin depth
$L$	55.3	system size in $x, y$ , and $z$ (except: if $B_{gz}/B_0 > 1$ , then $L_z/L = B_{gz}/B_0$ )

(N.B., Chernoglazov et al. 2023 includes 1% ultrarelativistic ions among positrons and electrons, with radiative cooling), although several 2D reconnection studies have (Melzani et al. 2014a, 2014b; Guo et al. 2016; Rowan et al. 2017; Ball et al. 2018, 2019; Werner et al. 2018; Rowan et al. 2019).

After describing the simulation setup (Section 2), we will focus on the different energy components, discussing the release of magnetic energy  $U_{B_{xy}}$  (Section 3), the increase in guide-field energy  $U_{B_z}$  (Section 4), the electric field energy  $U_E$  (Section 5), and the electron and ion energies  $U_e + U_i = U_{\text{ptcl}}$  (Section 6). We summarize in Section 7.

## 2. The Simulations

Simulations were run with the ZELTRON electromagnetic PIC code (Cerutti et al. 2013), initialized with semirelativistic electron–proton plasma in a standard Harris sheet configuration with uniform background plasma (similar to Werner et al. 2018)—initial physical and numerical parameters are listed in Table 1. By “semirelativistic” we mean that ions remain subrelativistic while electrons are ultrarelativistic and experience ultrarelativistic energy gains; in terms of quantities in Table 1,  $m_e c^2 \ll T_b \ll m_i c^2$  and  $\sigma_i \ll 1 \ll \sigma_e$ . The simulation frame (with zero initial electric field) is the zero-momentum

frame, where ions drift slowly and electrons carry the current supporting the field reversal.

The initial CS is perpendicular to  $y$ , with current in the  $+z$  direction and reversing magnetic field in the  $\pm x$  directions (approaching value  $B_0$  upstream). We add uniform guide field  $B_{gz}\hat{z}$ , exploring several strengths  $B_{gz}/B_0 \in \{0, 0.25, 0.5, 1, 2, 4\}$  (except  $B_{gz}/B_0 = 4$  was not run in 3D, due to expense). We also explore three dimensionalities: 2D $xy$  (2D simulation ignoring  $z$ —classic 2D reconnection), 2D $yz$  (ignoring  $x$ , for studying DKI), and full 3D. Also, in one case, 2D $yz$  and  $B_{gz} = 0$ , we ran an ensemble of three simulations, identical except for differing randomization of initial particles.

Table 2 lists length scales of interest in terms of  $\sigma_i\rho_{i0} = \sigma_e\rho_{e0}$ , where  $\rho_{s0} \equiv m_s c^2/(eB_0)$ ;  $\sigma_e\rho_{e0}$  is the gyroradius of an “energized” electron with energy  $2B_0^2/(8\pi n_{be})$  in perpendicular field  $B_0$ .

The system size, containing a single CS, is  $L \equiv L_y = 55.3\sigma_i\rho_{i0}$  and  $L_x = L_z = L$  (except when  $B_{gz} > B_0$ , we increase  $L_z = (B_{gz}/B_0)L_y$ ; and 2D simulations lack either the  $x$  or  $z$  dimension). Boundary conditions are periodic in  $x$  and  $z$ , and conducting/particle-reflecting in  $y$ . The size  $L$  is large with respect to initial kinetic scales and CS thickness (e.g.,  $L/(2\delta) = 83$ ), and  $L > 20\sigma_i\rho_{i0}$  puts it in the “large system

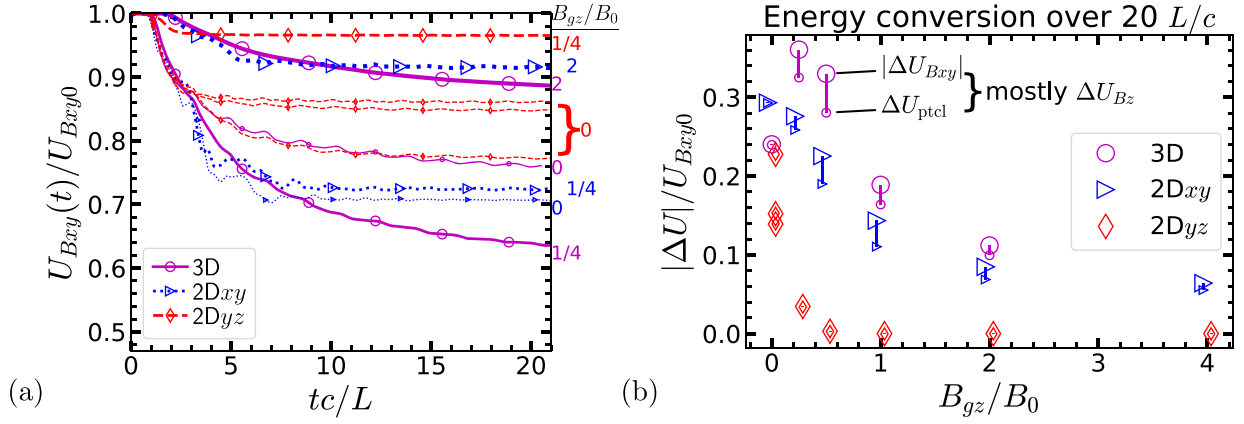


**Figure 1.** (a)  $U_{Bxy}(t)$  for selected simulations ( $B_{gz}$  is labeled for each). Three (differently seeded) 2Dyz simulations with  $B_{gz} = 0$  demonstrate the enhanced stochastic variability of DKI. (b)  $|\Delta U_{Bxy}|$  (large symbols) and  $\Delta U_{ptcl}$  (small symbols) vs.  $B_{gz}$ , normalized to  $U_{Bxy0}$ , the initial transverse magnetic energy.

regime” as defined by Werner et al. (2016), albeit for relativistic pair plasma in 2Dxy

We empirically found that using anisotropic grid cells with  $\Delta x/1.6 = \Delta y = \Delta z = \sigma_i \rho_{i0}/28$  avoids numerical instabilities while yielding the best computational performance. We similarly found that the number of computational macroparticles (each representing many physical particles) needed to avoid unphysical electron–ion energy exchange at late times was 160 per cell per species (with four species: background and CS electrons and ions) in 2D, whereas, in 3D, 10 macroparticles/cell/species sufficed.

No initial perturbation is used to kickstart reconnection, because such a perturbation (if uniform in  $z$ ) can significantly suppress 3D effects (Werner & Uzdensky 2021). Initial instabilities are therefore seeded by macroparticle noise.

### 3. Qualitative Evolution and Transverse Magnetic Energy Released

Over time, transverse magnetic energy  $U_{Bxy}$  is released to other forms ( $U_{Bxy}$  excludes energy in guide field  $B_z$ , which cannot be released—see Section 4). Figure 1(a) shows the evolution of  $U_{Bxy}(t)$  for selected simulations. Figure 1(b) shows the net loss in  $U_{Bxy}$  over  $T = 20L/c$  as a function of  $B_{gz}$ , for all simulations (large symbols). Ultimately this energy  $\Delta U_{Bxy}$  goes almost entirely to particles ( $\Delta U_{ptcl}$ , small symbols; see Section 6), with the small difference  $|\Delta U_{Bxy}| - \Delta U_{ptcl}$  comprising mainly  $\Delta U_{Bz}$ , which is the increase in guide-field energy (see Section 4).

In 2Dxy (Figure 1(a), blue triangles), magnetic energy decreases rapidly due to magnetic reconnection until saturation after  $5\text{--}10L/c$ . During that time we observe the familiar behavior of plasmoid-dominated reconnection. Reconnection pumps magnetic energy and flux from the upstream into plasmoids (magnetic islands), continually growing the total plasmoid volume and the magnetic energy therein. Apart from merging, plasmoids are permanent (stable) in 2D. Eventually (after  $5\text{--}10L/c$ ), in a closed system, the largest plasmoid becomes so large ( $\sim L$ ) that it halts reconnection—even though considerable transverse magnetic energy may remain upstream as well as in the plasmoid.

In 2Dyz (Figure 1, red diamonds), tearing and reconnection are forbidden, but the nonlinear DKI can rapidly release magnetic energy. We observe qualitatively similar behavior—the rippling of the CS, sometimes leading to a catastrophic

folding over on itself—as reported in nonrelativistic electron–ion plasma with artificially low  $m_i/m_e$  and in relativistic pair plasma (Ozaki et al. 1996; Pritchett & Coroniti 1996; Pritchett et al. 1996; Zhu & Winglee 1996; Zenitani & Hoshino 2007; Cerutti et al. 2014; Werner & Uzdensky 2021). The nonlinear DKI effectively thickens the CS, significantly slowing but not fully halting energy conversion. A DKI mode may enter the nonlinear stage when its rippling amplitude exceeds its rippling wavelength, but—like waves breaking in the ocean—whether and where this occurs has a substantial element of randomness (see Figures 28, 29, and 35 in Werner & Uzdensky 2021). While a large statistical study is beyond the scope of this work, this stochastic variation is shown via the three 2Dyz simulations with  $B_{gz} = 0$  (red diamonds and thin dashed lines) in Figure 1(a).

In 3D (Figure 1, magenta circles),  $U_{Bxy}$  can be released by reconnection and DKI. In addition, flux ropes (3D plasmoids) formed by reconnection may decay via the flux-rope kink instability, releasing still more magnetic energy than in 2D (Figure 1(b)). Because kinking flux ropes decay, reconnection will not halt as in 2Dxy, although CS thickening (due to DKI and flux-rope instability) slows both DKI and reconnection; all the 3D simulations in Figure 1(a) show continued but slow energy conversion beyond  $20L/c$  (Werner & Uzdensky 2021).

In Figure 1(b) we see that, for  $B_{gz} = 0$ , all dimensionalities yield comparable  $|\Delta U_{Bxy}| \sim 0.2\text{--}0.3U_{Bxy0}$ . While a small guide field  $B_{gz}/B_0 = 1/4$  has only a small effect in 2Dxy and 3D, it strongly inhibits energy conversion in 2Dyz (Zenitani & Hoshino 2008).

Increasing  $B_{gz}$  has two main effects, in all cases: it slows energy conversion, and decreases the net magnetic energy release  $|\Delta U_{Bxy}|$ . A guide field of  $B_{gz}/B_0 \gtrsim 1/2$  stabilizes the DKI in 2Dyz (see Zenitani & Hoshino 2008; Schoeffler et al. 2023), preventing any release of  $U_{Bxy}$ . For 2Dxy and 3D, increasing  $B_{gz}/B_0$  from 0 to 1 slows energy conversion and reduces  $|\Delta U_{Bxy}|$  by roughly half; by  $B_{gz}/B_0 = 2$ , only about  $0.1U_{Bxy0}$  is released (this depends on the aspect ratio: for  $L_y \gtrsim L_x$ , we expect  $|\Delta U_{Bxy}|/U_{Bxy0} \sim 0.1L_x/L_y$ ). Previous 2Dxy studies showed that  $B_{gz}$  slows reconnection by reducing the Alfvén speed  $v_{A,x}$  in the outflow direction (Liu et al. 2014; Werner & Uzdensky 2017); also,  $B_{gz}$  resists plasmoid compression, halting reconnection at smaller  $|\Delta U_{Bxy}|$ . These trends hold in 3D as well, except that increasing  $B_{gz}/B_0$  from 0 to  $1/4$  releases more energy, possibly because  $B_z$  suppresses the DKI and prevents interference with reconnection, or possibly

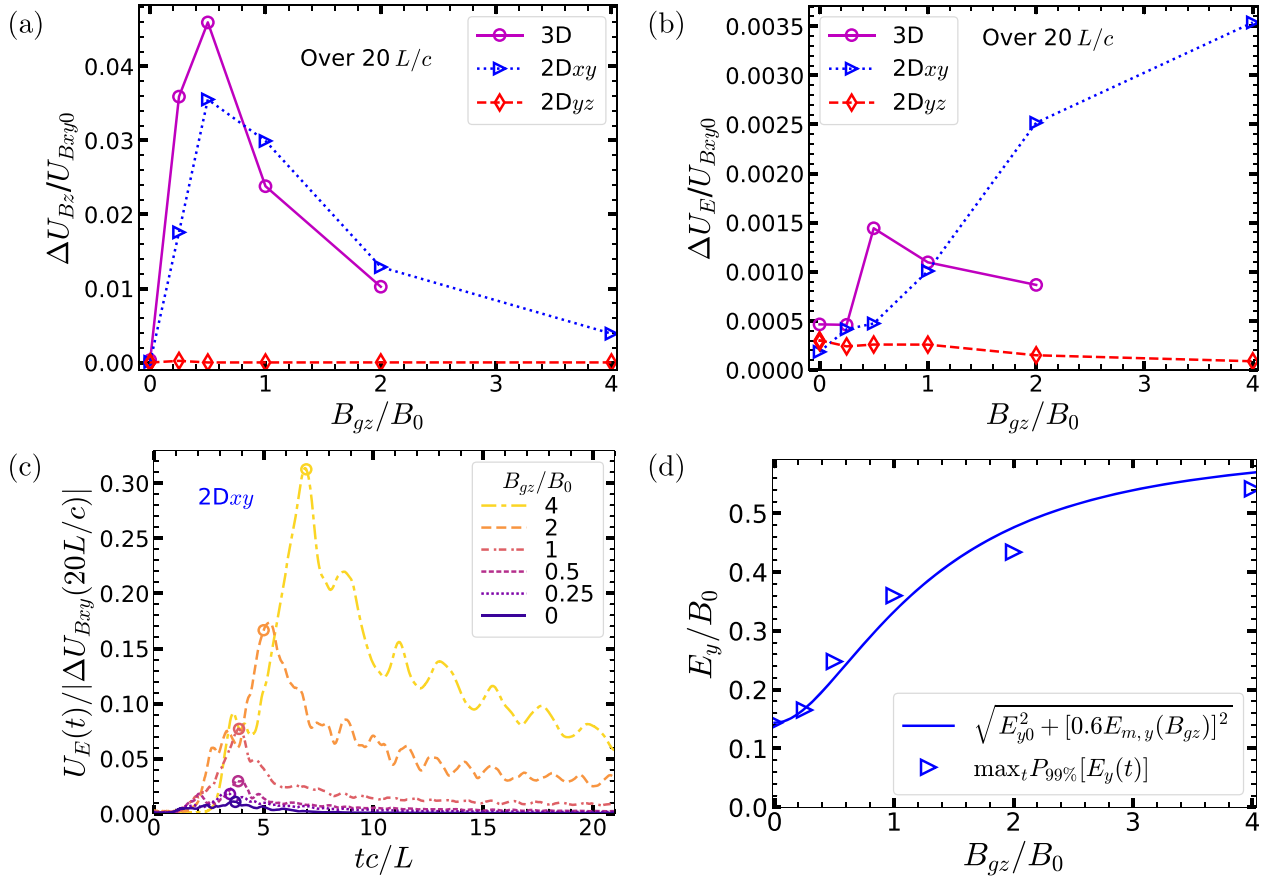


**Figure 2.** (a) Net gain in  $U_{Bz}$  vs.  $B_{gz}$ , in 2Dxy (blue triangles), 3D (magenta circles), and 2Dyz (red diamonds showing zero gain). (b) Net gain in  $U_E(B_{gz})$ . (c) For 2Dxy only,  $U_E(t)$  vs. time, for different  $B_{gz}$ , normalized to the ultimately released magnetic energy (not shown: in 2Dyz and 3D,  $U_E(t)$  remains relatively small).  $U_E$  dissipates only after most of  $U_{Bxy}$  has dissipated, as indicated by the circles placed where  $\Delta U_{Bxy}(t) = 0.75\Delta U_{Bxy}(20L/c)$ . (d) For 2Dxy, the plasmoid  $E_y$  as a function of  $B_{gz}$ , estimated from Equations (1)–(2) (solid line), compared with the maximum  $E_y$  measured in simulations (triangles). (To reduce sensitivity to noise, the maximum was measured over time of the 99th percentile of  $|E_y|$ .)

this is stochastic variation; we leave exploration of this subtrend to future work.

Overall, after  $20L/c$ ,  $\Delta U_{Bxy}$  is about 15% higher in 3D than in 2Dxy because 3D evolution accesses all the 2D dissipation channels plus the flux-rope instability; the difference between 2Dxy and 3D narrows slightly with higher  $B_{gz}$  as guide field increases uniformity in  $z$ . We note that with more time,  $|\Delta U_{Bxy}|$  would increase in 3D, but not in 2Dxy.

#### 4. Energy Gain in Guide Field

In our simulations, the guide-field energy  $U_{Bz}$  can only increase from its initial value; the  $B_z$ -flux through any  $x$ - $y$  plane is conserved and  $B_z$  is initially uniform, yielding the lowest  $U_{Bz}$  for the fixed flux. Figure 2(a) shows the net gain  $\Delta U_{Bz}$  versus  $B_{gz}$  for each dimensionality. In the 2Dyz case,  $\Delta U_{Bz} \approx 0$ , and for  $B_{gz} = 0$  neither 2Dxy nor 3D show noticeable gain. However, for  $B_{gz} > 0$ , reconnection outflows compress plasma and guide field in flux ropes, increasing  $U_{Bz}$ . The gain  $\Delta U_{Bz}$  increases with  $B_{gz}/B_0 \lesssim 0.5$  because there is more  $B_z$  to be compressed; however, stronger  $B_{gz}$  rivals the plasma in resisting compression (with adiabatic index 2, greater than the adiabatic index 4/3 or 5/3 of relativistic or nonrelativistic plasma; see Section 4.4 of Werner & Uzdensky 2021), and  $\Delta U_{Bz}$  peaks around  $0.04 U_{Bxy0}$  at  $B_{gz}/B_0 \sim 0.5$  before decreasing. The similarity between 2Dxy and 3D suggests reconnection occurs to similar extents—though slower in 3D—

resulting in similar compression of flux ropes, with energy remaining in  $U_{Bz}$  even as flux ropes decay in 3D.

We note that the contribution of the Hall quadrupole  $B_z$  field is negligible on global energy scales, because it is localized to small regions around X-lines; in contrast, the  $U_{Bz}$  in plasmoids becomes globally significant because it grows with plasmoids, which approach the system size.

#### 5. Energy Gain and Subsequent Loss in Electric Field

The net gain in electric field energy  $U_E$  is negligible in all cases—less than  $0.004 U_{Bxy0}$  (Figure 2(b)). For 2Dyz and 3D,  $U_E(t)$  is small at all times. However (see Figure 2(c)), in 2Dxy with strong guide field,  $U_E(t)$  builds up substantially over time before declining (after most reconnection has occurred); this effect increases with  $B_{gz}$ . For  $B_{gz}/B_0 = 2$ , 17% of the ultimately released magnetic energy resided at one time (around  $t = 5L/c$ ) in  $U_E$ , and for  $B_{gz}/B_0 = 4$ , over 30%.

This effect—by which substantial  $U_{Bxy}$  is first converted to  $U_E$  before energizing particles—has not been reported before, to our knowledge. We find that (when  $B_{gz}/B_0 \gtrsim 0.5$ )  $U_E$  is dominated by  $E_y$  in plasmoids; this is simply the motional electric field  $E_{m,y} \approx v_x B_z/c$  due to  $B_z$  in a plasmoid moving with relativistic speed  $v_x$  along the layer. This effect should appear in any 2D reconnection simulation with guide field and relativistic outflows, even in pair plasma. After the last major plasmoid merger, as reconnection is ending, only one large but stationary

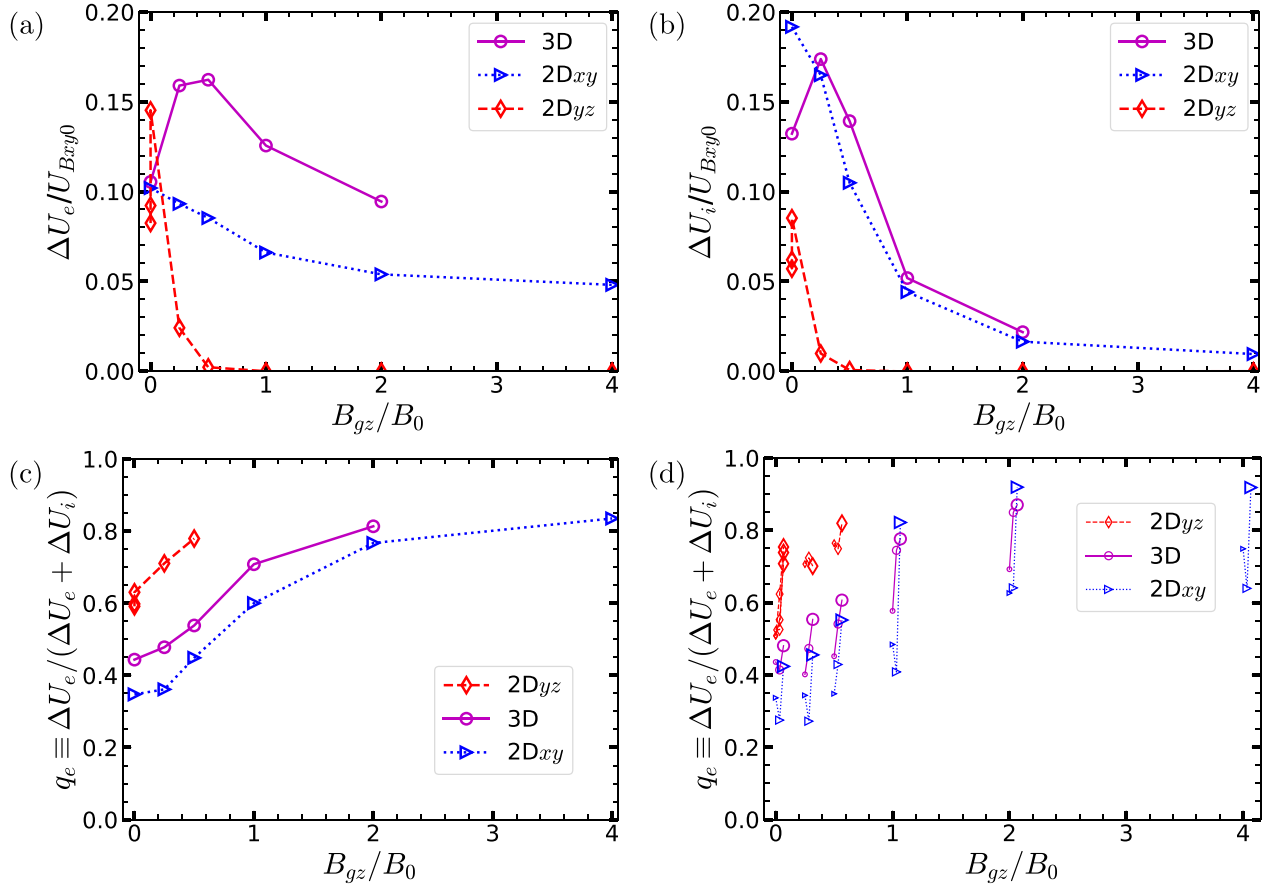


**Figure 3.** The net gain in (a) electron and (b) ion energy, vs.  $B_{gz}$ , normalized by initial transverse magnetic energy  $U_{B_{xy}0}$ , over the full  $T = 20 L/c$ . (c) The electron gain fraction  $q_e$  vs.  $B_{gz}$ . (d)  $q_e$  for each third (in terms of  $\Delta U_{B_{xy}}$ ) of each simulation (the smallest markers, shifted left, show  $q_e$  in the first third; the largest, shifted right, show the last third). 2D $yz$  cases with  $B_{gz}/B_0 > 0.5$ , hence negligible energization, are omitted.

plasmoid remains, and thus the motional electric field ultimately decays.

We can estimate how  $E_{m,y} \approx v_x B_z / c$  scales with guide field, assuming that  $B_z \sim B_{gz}$  and that plasmoid velocity  $v_x$  scales with  $v_{A,x}$ , the Alfvén velocity projected along  $x$ . Since the typical reconnection electric field is  $E_{\text{rec}} \sim 0.1 v_{A,x} B_0 / c$  (for fast collisionless reconnection),  $E_{m,y} / E_{\text{rec}} \sim 10 B_{gz} / B_0$ , which exceeds unity for even small  $B_{gz}$ . In absolute terms,  $v_{A,x} = c [B_0^2 / (4\pi h + B_0^2 + B_{gz}^2)]^{1/2}$ , where  $h$  is the relativistic plasma enthalpy density including rest mass (Liu et al. 2014; Sironi et al. 2016; Werner & Uzdensky 2017), and thus

$$E_{m,y}(B_{gz}) \sim \sqrt{\frac{B_{gz}^2 B_0^2}{4\pi h + B_0^2 + B_{gz}^2}} \rightarrow \begin{cases} E_{m,y} \propto B_{gz} & B_{gz}^2 \ll B_0^2 + 4\pi h \\ E_{m,y} \sim B_0 & B_{gz}^2 \gtrsim B_0^2 + 4\pi h \end{cases} \quad (1)$$

(In this paper,  $4\pi h \approx 4\pi n_b m_i c^2 = B_0^2 / \sigma_i = 2B_0^2$ .)

This estimate of  $E_{m,y}(B_{gz})$  roughly explains the  $B_{gz}$ -dependence of  $E_y$  in our 2D $xy$  simulations; Figure 2(d) shows the maximum observed  $E_y$  compared with

$$E_{y,\text{max}}(B_{gz}) = \sqrt{E_{y0}^2 + [\alpha E_{m,y}(B_{gz})]^2}, \quad (2)$$

which adds in quadrature the motional field  $E_{m,y}(B_{gz})$  given by Equation (1) and  $E_{y0} \equiv E_{y,\text{max}}(0) \approx 0.14 B_0$ , an estimate of  $E_y$  from other sources (which we measure in the simulation

with  $B_{gz} = 0$  and assume it remains similar for  $B_{gz} > 0$ ), with empirical factor  $\alpha \approx 0.6$  accounting for, e.g.,  $v_x < v_{A,x}$ .

Notably, when  $U_E$  dissipates at the end of reconnection, it preferentially energizes electrons, as described next.

## 6. Energy Gain in Electrons and Ions

In all dimensionalities, increasing guide field generally suppresses both electron and ion energization relative to the available magnetic energy  $U_{B_{xy}0}$  (Figures 3(a), (b)). In 2D $yz$ , both electron and ion net gains ( $\Delta U_e$  and  $\Delta U_i$ ) drop precipitously with  $B_{gz}$ . In 2D $xy$  and 3D, energy gains also fall, but not to zero, and  $\Delta U_i$  falls much faster than  $\Delta U_e$ . As  $B_{gz}/B_0$  increases from 0.25 to 2,  $\Delta U_e$  falls from  $0.09 U_{B_{xy}0}$  to  $0.05 U_{B_{xy}0}$  in 2D $xy$ , and from  $0.16 U_{B_{xy}0}$  to  $0.09 U_{B_{xy}0}$  in 3D; in contrast,  $\Delta U_i$  falls from about  $0.17 U_{B_{xy}0}$  to just  $0.02 U_{B_{xy}0}$  (almost an order of magnitude!), and is nearly identical in 2D $xy$  and 3D. The additional magnetic energy released in 3D (compared with 2D $xy$ ) goes mostly to electrons. At low  $B_{gz}$ , this may be due to the DKI and/or the flux-rope kink instability; at higher  $B_{gz}$ , DKI is quenched, suggesting that the flux-rope kink preferentially energizes electrons. The electron energy gain fraction  $q_e \equiv \Delta U_e / (\Delta U_e + \Delta U_i)$  grows with  $B_{gz}$  (Figure 3(c)), even though  $\Delta U_e$  decreases. In 2D $xy$ ,  $q_e \approx 0.35$  at  $B_{gz} = 0$ , increasing to  $q_e \approx 0.5$  (equipartition) around  $B_{gz}/B_0 = 0.75$ , and reaching  $q_e > 0.8$  by  $B_{gz}/B_0 = 4$ . In 3D,  $q_e(B_{gz})$  is higher than in 2D $xy$  by about 0.1 (though this gap narrows as  $B_{gz}$  increases), reaching equipartition near  $B_{gz}/B_0 = 0.25$ , and

$q_e \approx 0.7$  at  $B_{gz}/B_0 = 1$ . In 2Dyz,  $q_e$  is  $\sim 0.2$  higher than in 3D, but we emphasize that, for  $B_{gz}/B_0 \geq 0.5$ ,  $\Delta U_e$  in 2Dyz is tiny compared with 2Dxy and 3D (hence hard to measure).

The 3D case with  $B_{gz} = 0$  is exceptional, converting less energy than higher  $B_{gz}/B_0 = 0.25$ , but the difference is within the stochastic variation observed in 2Dyz for  $B_{gz} = 0$  (see Figures 1(b) and 3(a), (b)).

In the following, we compare  $q_e$  previously measured in 2Dxy PIC reconnection simulations in the (nearly) semi-relativistic, plasmoid-dominated regime. For  $B_{gz} = 0$ ,  $q_e \simeq 0.25\text{--}0.35$  was found in similar simulations (Rowan et al. 2017; Werner et al. 2018; Rowan et al. 2019; Zhang et al. 2021b) and also in the different regime of nonrelativistic laboratory experiment (e.g., Yamada et al. 2014). Similar increases in  $q_e$  with  $B_{gz}$  were also reported in 2D: e.g., Rowan et al. (2019) found  $q_e$  increasing to equipartition around  $B_{gz}/B_0 \approx 1$  and up to 0.92 for  $B_{gz}/B_0 = 6$ ; with reduced mass ratio  $\mu = 25$ , Melzani et al. (2014b) found  $q_e$  increasing to 0.67 at  $B_{gz}/B_0 = 1$ . There have, however, been no 3D PIC simulations in a quantitatively comparable regime (to our knowledge) that have measured  $q_e$ .

Although a detailed analysis of energization mechanisms is beyond the scope of this Letter, the time dependence of  $q_e$  offers some insight. Figure 3(d) plots  $q_e$  separately for each third (in terms of  $\Delta U_{Bxy}$ , not time) of each simulation. In 2Dyz, we observe no significant time dependence of  $q_e$ . For 2Dxy and strong  $B_{gz}$ , however, the last third (when  $U_E$  dissipates; see Figure 2(c)) has much higher  $q_e$  than the first two-thirds. Therefore, we conclude that energization by the motional electric field  $E_{m,y}$  differs from reconnection energization mechanisms that operate earlier (or without  $B_{gz}$ ), and yields higher  $q_e$ . In 3D, for strong  $B_{gz}$ , we see the last two-thirds have higher  $q_e$  than the first third, suggesting that  $U_E$  builds up a little in 3D, but is promptly dissipated. That is, energization via  $E_{m,y}$  operates continuously throughout 3D reconnection, but only at the end of 2Dxy reconnection due to the high integrity of plasmoids. Besides being useful in their own right, measurements of  $q_e$  can thus help distinguish between different energization mechanisms.

## 7. Summary

Using PIC simulation, we evolve a thin CS in 3D semirelativistic plasma (see Table 1), investigating energy conversion for different guide magnetic fields  $B_{gz}$ . The 3D simulations are compared with 2Dxy (reconnection) and 2Dyz (drift-kink) simulations with the same initial conditions.

We quantify the net changes in transverse and guide magnetic, electric, electron kinetic, and ion kinetic energies. We find the following:

1. Increasing  $B_{gz}$  slows energy conversion and reduces the total released magnetic energy.
2. Increasing  $B_{gz}$  suppresses ion energization more than electron energization, increasing  $q_e \equiv \Delta U_e / (\Delta U_e + \Delta U_i)$ . In 3D,  $\Delta U_e / U_{Bxy0}$  falls from 0.16 to 0.09 as  $B_{gz}/B_0$  increases from 0.25 to 2, while  $\Delta U_i / U_{Bxy0}$  falls from 0.17 to 0.02;  $q_e$  rises from roughly 0.5 to 0.8.
3. In 3D only, the flux-rope kink instability further energizes particles (mostly electrons), releasing the reconnected transverse magnetic energy stored in flux ropes, but not their guide-field energy (which is increased by compression during reconnection).



4. Relativistic reconnection in strong guide field transfers energy to transient motional electric fields  $E_{m,y}$  in flux ropes before preferentially energizing electrons. In 2Dxy,  $U_E$  grows substantially, and dissipates only at the end of reconnection; in 3D,  $U_E$  dissipates promptly, possibly due to flux-rope decay.
5. Different plasma processes operating in thin CSs yield different electron/ion energy partitions. We roughly distinguished electron energy fractions  $q_e$  due to four mechanisms: DKI, classic 2D reconnection, dissipation of  $E_{m,y}$ , and flux-rope kink instability. Their relative roles (especially for DKI and reconnection) in 3D may be sensitive to the CS configuration.

We have thus characterized the conversion of magnetic energy to electron and ion kinetic energy in 3D CSs, addressing a fundamental plasma-physics question and obtaining new insight into the interplay of multiple dissipation channels yielding different energization of electrons versus ions. Importantly, we measured, from first-principles simulation, electron and ion heating fractions critical for subgrid modeling of electron energization (e.g., Dexter et al. 2020; Scepi et al. 2022), and we showed that they depend significantly on the guide magnetic field. These results, in combination with similar studies in the 3D relativistic pair-plasma regime (e.g., Yin et al. 2008; Zenitani & Hoshino 2008; Liu et al. 2011; Kagan et al. 2013; Cerutti et al. 2014; Guo et al. 2014, 2021; Sironi & Spitkovsky 2014; Werner & Uzdensky 2017; Zhang et al. 2021a; Werner & Uzdensky 2021), will be important in connecting magnetic energy dissipation with particle energization and observed radiation in the complex and varied environment of accreting BHs.

## Acknowledgments

This work was supported by NSF grants AST-1806084 and AST-1903335 and by NASA grants 80NSSC20K0545 and 80NSSC22K0828. The 3D simulations used computer time provided by the U.S. Department of Energy's (DOE) Innovative and Novel Computational Impact on Theory and Experiment (INCITE) Program, and in particular used resources from the Argonne Leadership Computing Facility, a U.S. DOE Office of Science user facility at Argonne National Laboratory, which is supported by the Office of Science of the U.S. DOE under Contract No. DE-AC02-06CH11357. The 2D simulations were run on the Frontera supercomputer at the Texas Advanced Computing Center (TACC) at The University of Texas at Austin.

## ORCID iDs

Gregory R. Werner  <https://orcid.org/0000-0001-9039-9032>  
Dmitri A. Uzdensky  <https://orcid.org/0000-0001-8792-6698>

## References

- Bacchini, F., Arzamassiy, L., Zhankin, V., et al. 2022, *ApJ*, 938, 86  
Ball, D., Sironi, L., & Özel, F. 2018, *ApJ*, 862, 80  
Ball, D., Sironi, L., & Özel, F. 2019, *ApJ*, 884, 57  
Cerutti, B., Werner, G. R., Uzdensky, D. A., & Begelman, M. C. 2013, *ApJ*, 770, 147  
Cerutti, B., Werner, G. R., Uzdensky, D. A., & Begelman, M. C. 2014, *ApJ*, 782, 104  
Chael, A., Rowan, M., Narayan, R., Johnson, M., & Sironi, L. 2018, *MNRAS*, 478, 5209

- Chashkina, A., Bromberg, O., & Levinson, A. 2021, *MNRAS*, 508, 1241
- Chernoglazov, A., Hakobyan, H., & Philippov, A. 2023, *ApJ*, 959, 122
- Daughton, W. 1999, *JGR*, 104, 28701
- Dexter, J., Jiménez-Rosales, A., Ressler, S. M., et al. 2020, *MNRAS*, 494, 4168
- Galeev, A., Rosner, R., & Vaiana, G. 1979, *ApJ*, 229, 318
- Guo, F., Li, H., Daughton, W., & Liu, Y.-H. 2014, *PhRvL*, 113, 155005
- Guo, F., Li, X., Daughton, W., et al. 2021, *ApJ*, 919, 111
- Guo, F., Li, X., Li, H., et al. 2016, *ApJL*, 818, L9
- Guo, F., Liu, Y.-H., Daughton, W., & Li, H. 2015, *ApJ*, 806, 167
- Hankla, A. M., Scepti, N., & Dexter, J. 2022, *MNRAS*, 515, 775
- Hesse, M., & Birn, J. 2000, *GMS*, 118, 295
- Kagan, D., Milosavljević, M., & Spitkovsky, A. 2013, *ApJ*, 774, 41
- Liu, W., Li, H., Yin, L., et al. 2011, *PhPI*, 18, 052105
- Liu, Y.-H., Daughton, W., Karimabadi, H., Li, H., & Peter Gary, S. 2014, *PhPI*, 21, 022113
- Markidis, S., Lapenta, G., Delzanno, G. L., et al. 2014, *PPCF*, 56, 064010
- Melzani, M., Walder, R., Folini, D., Winisdoerffer, C., & Favre, J. M. 2014a, *A&A*, 570, A111
- Melzani, M., Walder, R., Folini, D., Winisdoerffer, C., & Favre, J. M. 2014b, *A&A*, 570, A112
- Ozaki, M., Sato, T., Horiuchi, R. & Complexity Simulation Group 1996, *PhPI*, 3, 2265
- Pritchett, P. L., & Coroniti, F. V. 1996, *JGG*, 48, 833
- Pritchett, P. L., Coroniti, F. V., & Decyk, V. K. 1996, *JGR*, 101, 27413
- Ressler, S. M., White, C. J., Quataert, E., & Stone, J. M. 2020, *ApJL*, 896, L6
- Ressler, S. M., White, C. J., & Quataert, E. 2023, *MNRAS*, 521, 4277
- Ripperda, B., Bacchini, F., & Philippov, A. A. 2020, *ApJ*, 900, 100
- Rowan, M. E., Sironi, L., & Narayan, R. 2017, *ApJ*, 850, 29
- Rowan, M. E., Sironi, L., & Narayan, R. 2019, *ApJ*, 873, 2
- Scepti, N., Dexter, J., & Begelman, M. C. 2022, *MNRAS*, 511, 3536
- Schoeffler, K. M., Grismayer, T., Uzdensky, D., & Silva, L. O. 2023, *MNRAS*, 523, 3812
- Scholer, M., Sidorenko, I., Jaroschek, C. H., Treumann, R. A., & Zeiler, A. 2003, *PhPI*, 10, 3521
- Sironi, L., Giannios, D., & Petropoulou, M. 2016, *MNRAS*, 462, 48
- Sironi, L., & Spitkovsky, A. 2014, *ApJL*, 783, L21
- Uzdensky, D. A., & Goodman, J. 2008, *ApJ*, 682, 608
- Werner, G. R., & Uzdensky, D. A. 2017, *ApJL*, 843, L27
- Werner, G. R., & Uzdensky, D. A. 2021, *JPIPh*, 87, 905870613
- Werner, G. R., Uzdensky, D. A., Begelman, M. C., Cerutti, B., & Nalewajko, K. 2018, *MNRAS*, 473, 4840
- Werner, G. R., Uzdensky, D. A., Cerutti, B., Nalewajko, K., & Begelman, M. C. 2016, *ApJL*, 816, L8
- Yamada, M., Yoo, J., Jara-Almonte, J., et al. 2014, *NatCo*, 5, 4774
- Yin, L., Daughton, W., Karimabadi, H., et al. 2008, *PhRvL*, 101, 125001
- Zenitani, S., & Hoshino, M. 2005, *PhRvL*, 95, 095001
- Zenitani, S., & Hoshino, M. 2007, *ApJ*, 670, 702
- Zenitani, S., & Hoshino, M. 2008, *ApJ*, 677, 530
- Zhang, H., Sironi, L., & Giannios, D. 2021a, *ApJ*, 922, 261
- Zhang, Q., Guo, F., Daughton, W., Li, H., & Li, X. 2021b, *PhRvL*, 127, 185101
- Zhdankin, V., Ripperda, B., & Philippov, A. A. 2023, *PhRvR*, 5, 043023
- Zhu, Z., & Winglee, R. M. 1996, *JGR*, 101, 4885
- Zweibel, E. G., & Yamada, M. 2009, *ARA&A*, 47, 291